

1 **Combined THEMIS and ground-based observations of a pair of**
2 **substorm associated electron precipitation events**

3
4 Mark A. Clilverd

5 British Antarctic Survey, Cambridge, United Kingdom.

6 Craig J. Rodger

7 Department of Physics, University of Otago, Dunedin, New Zealand.

8 I. Jonathan Rae

9 Department of Physics, University of Alberta, Edmonton, Canada.

10 James B. Brundell, Neil R. Thomson

11 Department of Physics, University of Otago, Dunedin, New Zealand.

12 Neil Cobbett

13 British Antarctic Survey, Cambridge, United Kingdom.

14 Pekka T. Verronen

15 Finnish Meteorological Institute, Helsinki, Finland.

16 Frederick W. Menk

17 University of Newcastle, Callaghan, Australia.

18
19 **Abstract.** Using ground-based subionospheric radio wave propagation data from two VLF
20 receiver sites, riometer absorption data, and THEMIS satellite observations we examine in detail
21 energetic electron precipitation (EEP) characteristics associated with two substorm precipitation
22 events that occurred on 28 May 2010. In an advance on the analysis undertaken by Clilverd et al.
23 [2008] we use phase observations of VLF radio wave signals to describe substorm-driven EEP
24 characteristics more accurately than before. Using a >30 keV electron precipitation flux of

25 $5.6 \times 10^7 \text{ el.cm}^{-2} \text{ sr}^{-1} \text{ s}^{-1}$ and a spectral gradient consistent with that observed by THEMIS, it was
26 possible to accurately reproduce the peak observed riometer absorption at Macquarie Island
27 ($L=5.4$), and the associated NWC radio wave phase change observed at Casey, Antarctica during
28 the second, larger, substorm. The flux levels were near to 80% of the peak fluxes observed in a
29 similar substorm as studied by Clilverd et al. [2008]. During the initial stages of the second
30 substorm a latitude region of $5 < L < 9$ was affected by electron precipitation. Both substorms
31 showed expansion of the precipitation region to $4 < L < 12$ >30 minutes after the injection. While
32 both substorms occurred at similar local times, with electron precipitation injections into
33 approximately the same geographical region, the second expanded in eastward longitude more
34 slowly, suggesting the involvement of lower energy electron precipitation. Each substorm region
35 expanded westwards at a rate slower than that exhibited eastwards. This study shows that it is
36 possible to successfully combine these multi-instrument observations to investigate the
37 characteristics of substorms.

38

39

40 **1. Introduction**

41 Understanding the morphology of energetic electron precipitation (EEP) into the atmosphere is
42 an important requirement, both in determining the role of electron losses from the
43 magnetosphere [Spanswick et al., 2007; Clilverd et al., 2008; Reeves et al., 2009], and the
44 subsequent impact of EEP on the atmosphere [e.g., Seppala et al., 2007; 2009]. Much is already
45 known about the timescales of EEP, with precipitation events occurring over seconds [Lorentzen
46 et al., 2001; Rodger et al., 2007b], minutes [Millan et al., 2002; Rodger et al., 2008], hours
47 [Kavanagh et al., 2007; Spanswick et al., 2007; Clilverd et al., 2008], and days [Rodger et al.,
48 2007c; Clilverd et al., 2010]. What is less well known about these events is the precipitation flux
49 and energy spectrum involved. Detailed knowledge of these parameters would allow more
50 accurate analysis of the role of EEP on magnetospheric loss processes, and also the way EEP
51 couples into the atmosphere.

52 Accurate measurements of EEP are difficult to make from spacecraft at high altitudes because
53 the bounce loss cone is small at these locations and thus hard to resolve, while at low altitudes
54 the detectors either measure only a fraction of the bounce loss cone, or include some of the drift
55 loss cone, and occasionally some of the trapped component of the radiation belts [Rodger et al.,
56 2010a]. Some current spacecraft measure only a fraction of the bounce loss cone, with poor
57 energy resolution, but reasonable spatial coverage (e.g., SAMPEX and POES). Some have poor
58 energy resolution, and do not resolve the bounce loss cone, but do have constant limited spatial
59 coverage (e.g., GOES and LANL). Others do not resolve the bounce loss cone, but do have
60 reasonable spatial coverage, and have good energy resolution (e.g., DEMETER and THEMIS).

61 Ground-based measurements of EEP characteristics rely on monitoring the changes in D-
62 region ionisation caused by the precipitation. Techniques effectively use the ionosphere as a
63 large particle detector [Clilverd et al., 2009], but they suffer from significant limitations as a
64 result of the combination of both EEP energy spectra and precipitation flux being important

65 factors in determining the production of the D-region ionisation. Only by using multi-parameter,
66 and multi-instrument observations of the ionisation changes produced by EEP is it possible to
67 accurately characterise the EEP events. The combination of ground-based and satellite
68 measurements provides the clearest morphology of EEP characteristics, and this work builds on
69 previous studies of this kind [e.g., Clilverd et al., 2008; Clilverd et al., 2010].

70 Substorms generate EEP through the conversion of solar wind energy stored in the Earth's
71 magnetotail into particle heating and kinetic energy [Akasofu, 1964; Axford, 1999; Liu et al.,
72 2009a]. The reconfiguration of the magnetosphere generates earthward and tailward flows
73 centred on a reconnection site at $\sim 20\text{-}30 R_E$ in the magnetotail [Nagai et al., 1998; Liu et al.,
74 2009a]. Liu et al. [2009b] successfully modelled an observed substorm injection of energetic
75 particles propagating radially inward towards geosynchronous orbit. The model consisted of an
76 earthward dipolarization-like pulse from the magnetotail located beyond $20 R_E$, and reproduced
77 most features of the injected particles, including the timing of the injection as observed by
78 different satellites. Liu et al. [2009b] observed magnetic field dipolarization signatures at \sim
79 $11 R_E$ to occur ~ 90 s after tail reconnection signatures at $\sim 20 R_E$. Spanswick et al. [2009]
80 studied a substorm on 27 August 2001 in detail, concluding that the magnetic field pulse took
81 ~ 8 minutes to propagate from $-18 R_E$ to $-6.6 R_E$. Spanswick et al. [2009] also reported that EEP
82 were observed on the ground near $L=6.6$ and expanded both polewards and equatorwards –
83 consistent with the earlier riometer-based survey of Berkey et al. [1974].

84 Typically, EEP from a substorm injection occurs near MLT midnight, with the precipitation
85 region (in the ionosphere) rapidly expanding eastwards with velocities that correspond to
86 electron drift velocities associated with energies of 50-300 keV [Berkey et al. 1974]. The
87 electron energies involved in substorm injections seen by satellites such as LANL are typically
88 50-1000 keV, with the highest fluxes occurring at the lowest energies [Baker et al., 1985;
89 Clilverd et al., 2008]. While the satellite observations provide some information on the energy

90 spectra of the injected electrons, and the fluxes in drift orbit, it is very difficult to determine what
91 proportion of the electrons are being precipitated into the atmosphere through onboard satellite
92 measurements. The primary difficulty is in making observations of electron populations in the
93 spatially narrow loss cone in the magnetosphere, particularly around the geomagnetic equator
94 where geostationary satellites reside.

95 Energetic electron precipitation during substorms has been studied using riometers [e.g., Jelly
96 and Brice, 1967], forward scatter radar [e.g., Bailey, 1968], and VLF radio waves [e.g., Thorne
97 and Larsen, 1976]. Riometers observe an absorption maximum which is located close to 65°
98 geomagnetic latitude ($L \sim 6$) but which expands poleward and equatorwards within 15 minutes to
99 cover a latitude range of $60\text{-}73^\circ$ geomagnetic ($L=4\text{-}12$). This latitude range is consistent with the
100 observations from particle detectors on DMSP flights [Sandholt et al., 2002]. The VLF radio
101 wave technique is most sensitive to ionization caused by high energy and relativistic electron
102 precipitation energies, typically >100 keV, as these energies ionize the neutral atmosphere in the
103 Earth-ionosphere waveguide i.e., at altitudes below ~ 70 km [Barr et al., 2000]. The energy
104 spectrum of substorm-driven electron precipitation into the atmosphere was determined using
105 high altitude balloon measurements of X-ray fluxes, was been found to be of the same form as
106 the trapped fluxes [Rosenberg et al., 1972].

107 In a previous study Clilverd et al. [2008] used amplitude-only VLF subionospheric radio wave
108 data from a high latitude locations ($L=999$, Casey, Australian Antarctic Division) and electron
109 fluxes from the geostationary satellite LANL-97A, all in the region south of Australia and New
110 Zealand, to describe and model electron precipitation driven by substorm injection events. The
111 energy spectrum observed by the LANL-97A instrument during substorms was used to
112 accurately model the subionospheric radiowave substorm signature seen on the VLF transmitter
113 (NWC, Australia) received at Casey, as well as the substorm-driven riometer absorption levels
114 seen at Macquarie Island ($L=5.4$, Australian Antarctic Division). The maximum precipitation rate

115 into the atmosphere was found to be 50%-90% of the peak fluxes measured by the LANL-97A
116 spacecraft.

117 The enhanced ionisation caused by EEP can produce odd nitrogen (NO_x) and odd hydrogen
118 (HO_x) species in the upper and middle atmosphere [Brasseur and Solomon, 2005]. HO_x is short
119 lived but responsible for the catalytic ozone loss at mesospheric altitudes [Verronen et al., 2011],
120 while NO_x is much longer lasting in the absence of sunlight, and can be transported to lower
121 altitudes where it can catalytically destroy ozone in the stratosphere, particularly at the poles
122 [Randall et al., 2005; Seppala et al., 2009]. The altitude and concentrations of NO_x and HO_x
123 produced by EEP is a function of the precipitating electron energy spectrum and flux levels that
124 occur during the precipitation events. Precipitation processes generate a wide range of energy
125 spectra and flux levels, all contributing to the altitude profiles of NO_x and HO_x concentrations at
126 any given time. Radiation belt processes during enhanced geomagnetic activity have been shown
127 to generate EEP in large enough amounts to cause observable chemical changes in the upper
128 atmosphere [Verronen et al., 2011]. Radiation belt processes can generate EEP for long periods
129 (~10 days) which also contributes to their chemical effect in the atmosphere [Rodger et al.,
130 2010b; Clilverd et al., 2010]. In contrast, substorm-driven EEP is short lived, but can generate
131 EEP with higher fluxes at <500 keV than some radiation belt processes [Clilverd et al., 2008]. As
132 such, it is important that the characteristics of substorm-driven EEP are understood in detail.

133 In this study we examine the electron precipitation characteristics from two substorm injection
134 events on 28 May 2010, observed in ground-based data and from the THEMIS E satellite. In an
135 advance on the analysis of substorm EEP effects undertaken by Clilverd et al. [2008] which used
136 similar techniques and datasets, here we use phase observations of VLF radio wave signals, in
137 addition to two receiver sites instead of one, and investigate the time evolution of the substorm
138 EEP instead of restricting ourselves to only the peak fluxes. **Highly variable winter-nighttime**
139 **amplitude values make it difficult to accurately determine the undisturbed behaviour, and**

140 therefore accurately determine any substorm effect using amplitude alone. However, during the
141 nighttime, phase values are relatively steady in undisturbed conditions, and as such we
142 concentrate on the analysis of phase measurements for this study. Also, we expect near-linear
143 phase responses to EEP flux variations rather than the more complex patterns of amplitude
144 behaviour as identified in Figure 5 of Clilverd et al. [2008]. As a result of using phase
145 measurements instead of amplitude, we are able to describe substorm-driven EEP more
146 accurately than before.

147

148 2. Experimental setup

149 This study builds on previous work [Clilverd et al., 2008] using Very Low Frequency radio
150 wave observations. Receiver sites are part of the Antarctic-Arctic Radiation-belt Dynamic
151 Deposition VLF Atmospheric Research Konsortia [Clilverd et al., 2009]. Each receiver is
152 capable of receiving multiple narrow-band transmissions from powerful man-made
153 communication transmitters. The AARDDVARK network uses narrow band subionospheric
154 VLF/LF data spanning 10-40 kHz to observe changes in the D-region ionisation levels. This
155 study makes use of the transmissions from NWC (19.8 kHz, 21.8°S, 114.1°E, $L=1.44$), NPM
156 (21.4 kHz, 21.4°N, 158.1°W, $L=1.17$) and NLK (24.8 kHz, 48.2°N, 121.9°W, $L=2.92$) received
157 at Casey, Antarctica (66.3°S, 110.5°E, $L>999$) and Scott Base, Antarctica (77.8°S, 166.8°E,
158 $L>32$). The transmitter to receiver subionospheric great circle paths (GCP) are shown in Figure 1
159 as solid lines. Also plotted are the L -shell contours for $L=4$, 6 and 12. The effects of changing
160 propagation conditions in the mesosphere, often due to energetic particle precipitation can be
161 seen as either an increase or decrease in signal amplitude, and typically an increase in phase,
162 depending on the modal mixture of each signal observed [Barr et al., 2000].

163 The location of the southern hemisphere footprint of the THEMIS E satellite from about
164 11:30-13:30 UT on 28 May 2010 is also shown in Figure 1. The magnetic field model used the
165 IGRF for the internal component, with the Tsyganenko 89C external field, and Kp set to 3. The
166 location is plotted because we analyse the data from THEMIS E later in this paper, as part of a
167 case study. THEMIS E is part of a multi-spacecraft mission to study substorms. THEMIS
168 consists of five identical satellites equipped with particle and field instrumentation, including the
169 Solid State Telescope (SST). The SST instrument on THEMIS measures energetic electron
170 populations in the energy range 25-900 keV, providing observations centered on several
171 channels, i.e., 30, 41, 53, 67, 95, 143, 207, 297, 422, and 655 keV [Angelopoulos, 2008]. We

172 note here that THEMIS SST uses an attenuator when passing through the radiation belts in order
173 to protect the instrument. The data presented in this study has the attenuator in operation and thus
174 the inter-calibration of energetic electron energy fluxes from the individual energy channels is
175 uncertain at this time [Angelopoulos, personal communication, 2011].

176 The riometer data used in this study are provided from Macquarie Island (54.5°S, 158.9°E,
177 $L=5.4$). The riometer is a widebeam, 30 MHz, vertical pointing parallel dipole system, with time
178 resolution of 1 minute. Riometers [Little and Leinbach, 1959] observe the integrated absorption
179 of cosmic radio noise through the ionosphere, with increased absorption due to additional
180 ionization, for example due to both proton and electron precipitation. The dominant altitude of
181 the absorption is typically in the range 70-100 km, i.e., biased towards relatively soft particle
182 energies (~ 30 keV electrons). The co-location of the Macquarie Island riometer in L-shell and
183 longitude with the THEMIS E southern hemisphere magnetic field-line footprint in Figure 1
184 should be noted.

185

186 **3. Results**

187 Previous published results from the AARDDVARK system at Casey presented only amplitude
188 measurements from NWC [Clilverd et al., 2008]. Following an upgrade in February 2009, and
189 the December 2008 installation of an additional system at Arrival Heights, Scott Base,
190 Antarctica, we are able to analyse NWC phase measurements for the first time. Typically we
191 expect near-linear phase responses to EEP flux variations rather than the more complex patterns
192 of amplitude behaviour as identified in Figure 5 of Clilverd et al. [2008]. Figure 2 of the current
193 paper shows three examples of the NWC nighttime phase variation at Casey (upper panel) and
194 Scott Base (lower panel). The solid lines represent the nighttime data on 28 June 2009, 30 August
195 2009, and 28 May 2010 as labelled. The dotted lines represent the typical undisturbed behaviour
196 of the phase, taken from geomagnetically quiet days close to the event days. The undisturbed

197 phase behaviour shows a decrease in phase during sunset conditions on the propagation path
198 (starting at ~09 UT in the Figure), and an increase in phase during sunrise conditions (starting at
199 ~22 UT in the Figure). During the nighttime (~13-22 UT) the phase is relatively steady, and
200 typically ~400° lower than during daytime. At 17 UT on 28 June 2009, 16 UT on 30 August
201 2009, and 12 UT on 28 May 2010, phase increases of ~ 200° are observed at Casey, with
202 corresponding changes of ~40° at Scott Base. The enhancement of phase during these EEP
203 events typically lasts 1-3 hours, with the phase returning to near undisturbed values by the end of
204 the events. There are also NWC amplitude measurements available during these events, but
205 highly variable winter-nighttime amplitude values make it difficult to accurately determine the
206 undisturbed behaviour, and as such we concentrate on phase measurements for this study.

207 For one of the events shown, ~12 UT on 28 May 2010, the southern hemisphere footprint of
208 the magnetic field line on which the THEMIS E spacecraft was located was close to the great
209 circle paths between the NWC transmitter and the two receivers. Because of the extra detail that
210 THEMIS can provide in terms of magnetic field measurements, and in-situ observations of outer
211 radiation belt electron populations [Angelopoulos, 2008], we concentrate on the 28 May 2010
212 event in detail for the remainder of this paper. Figure 3 shows the underlying geophysical
213 conditions that were occurring around 28 May 2010. Panels in this figure show the variation of
214 solar wind speed, Dst, Kp, and GOES >10 MeV proton fluence for 27 – 29 May 2010. A small,
215 but sudden increase in solar wind speed at ~02 UT on 28 May 2010 led to a small geomagnetic
216 storm with the main phase occurring on 29 May 2010 as evidenced by $Dst \approx -100$, and $Kp=5$.
217 During 28 May 2010 Kp increased gradually from very quiet levels to a slightly disturbed state
218 ($Kp = 0$ to 3), and Dst became positive, with the solar wind remaining slightly elevated
219 ($\sim 400 \text{ km s}^{-1}$). The lack of any change in the solar proton fluence panel indicates there was no

220 solar proton event associated with this storm. These conditions are consistent with the **initial**
221 phase of a geomagnetic storm.

222 In Figure 4 we show the THEMIS E data during the 28 May 2010 event. The plot covers 10-
223 14 UT. At this time THEMIS E was within 1° of the geomagnetic equator on the $L\sim 5.5$ field-
224 line, and the southern hemisphere footprint of the magnetic field-line passing through the
225 satellite was in close proximity to the location of the Macquarie Island riometer (shown in Figure
226 1). This fortunate arrangement allows us to make detailed comparisons between the observations
227 made by THEMIS E and the ground-based instrumentation. The upper panel shows the THEMIS
228 SST electron flux variations for a number of energy ranges, and indicates two periods of
229 enhanced fluxes, one starting at 11:36 UT, peaking at 11:50 UT, and the second at 12:20 UT,
230 peaking at 12:30 UT. **The middle panel shows the same two periods of enhanced fluxes but as a**
231 **function of >30 keV integrated energy flux.** The lower panel shows the 3-component magnetic
232 field measurements **in Geocentric Solar Ecliptic (GSE) coordinates** for the same period. The
233 reversal of the x and z magnetic field components between 11:36 UT and 12:20 UT are
234 indicative of two sequential substorm activations which show the increase in Z and decrease in
235 X-component of a dipolarization [Lopez and Liu, 1990] as the magnetic field changes from tail-
236 like to dipole-like. The largest fluxes observed by THEMIS E are seen after the second
237 activation, from 12:20-13:30 UT, with elevated fluxes occurring in the energy range from 25-
238 200 keV.

239 The responses of the NWC signals received at Casey and Scott Base during 10-16 UT on 28
240 May 2010 are shown in the upper and middle panels of Figure 5. Vertical dash-dot lines indicate
241 the timing shown by THEMIS observations in Figure 4, namely first substorm activation time of
242 11:36 UT, and the second substorm activation time of 12:20 UT. The NWC-Casey phase
243 variation shows two enhancements, the initial smaller event coincides with the first THEMIS
244 substorm activation at $\sim 11:36$ UT but starting **~ 15 minutes** earlier, and which shows phase

245 changes of $\sim 100^\circ$. The largest NWC phase change seen at Casey begins at $\sim 12:20$ UT, shows a
246 double peaked structure, initially at 12:30 UT with peak values of $\sim 208^\circ$, eventually maximising
247 at 12:51 UT with phase change values of 265° . At Scott Base there is no obvious phase change
248 associated with the first THEMIS substorm activation, but a gradual phase change starts at about
249 11:50 UT, a small peak at 12:10 UT followed by a larger peak at about 12:30 UT. A comparison
250 of the phase variations between Casey and Scott Base suggests that they follow a similar pattern,
251 but with NWC-Scott Base leading the NWC-Casey substorm signature by about 20 minutes.
252 However, the most likely explanation of these two datasets is that the NWC-Scott Base substorm
253 signature is due to the first substorm, not the second, and thus the peak phase effects appear
254 delayed by ~ 34 minutes. This delay is difficult to explain as at the substorm injection L -shells
255 ($L \sim 6$) the NWC-Scott Base propagation path lies between NWC-Casey and the locations of
256 Macquarie Island and the THEMIS magnetic field line footprint (see Figure 1). At 14:04 UT
257 there was a NWC off-air period lasting for ~ 0.5 hour. The timing of this in both the Casey and
258 Scott Base NWC records indicates that the instrument clocks were accurate to < 1 s during this
259 period.

260 The variation in absorption from the Macquarie Island riometer, situated at a similar L -shell to
261 the THEMIS observations, is plotted in the lower panel of Figure 5. As above, the timing of the
262 THEMIS E substorm activation events shown in the upper panel of Figure 4 are indicated by
263 vertical dot-dashed lines. The absorption shows a small increase following the start of the first
264 THEMIS substorm activation, and a larger increase at the time of the second activation, peaking
265 at 12:30 UT with ~ 3.2 dB of absorption. Following the second peak, the absorption gradually
266 recovers to near zero levels at about the same time as the end of the second THEMIS substorm
267 event. It is clear from this figure that the variation in riometer absorption is consistent with the
268 variation in THEMIS E flux observations made at similar L -shells and similar longitudes.

269 Further, the timing of the peak absorption is co-incident with the first of the two large peaks in
270 NWC phase change observed at Casey, i.e., at 12:30 UT.

271 Thus what we observe in this event are two substorm activations well described by THEMIS E
272 measurements when the satellite is located on field-lines close to Macquarie Island. The first
273 substorm shows smaller flux enhancements than the second. The Macquarie Island riometer
274 responds with a similar temporal variation compared with THEMIS, again with lower absorption
275 enhancement during the first substorm compared with the second. The Casey NWC phase
276 change shows some response at the time of the first and second substorms, with the second
277 substorm peak phase effect larger than the first substorm. However a further large change in
278 NWC-Casey phase occurs after both the THEMIS particle detectors, and the Macquarie Island
279 riometer have begun to recover back to non-disturbed levels during the second substorm, with
280 NWC-Casey peaking about 25 minutes later. NWC-Scott Base phase changes show no
281 immediate response to the first substorm activation, but thereafter show a double peaked
282 behaviour that is similar to NWC-Casey but in advance of it by about 20 minutes. Clearly the
283 NWC-Scott Base phase behaviour is most likely to be associated with the first substorm, but the
284 temporal evolution of the substorm precipitation region is unclear at this stage. The aim for this
285 study is therefore to determine the relationship between the EEP fluxes observed by the ground-
286 based instruments and those observed by the THEMIS E satellite, to answer why there are
287 differences in response between the instruments during these substorms, and therefore why there
288 are differences in the timing of the observed features.

289

290 **4. Discussion**

291 **4.1 Modelling the EEP flux**

292 In this subsection we model the effect that the substorm-driven EEP has on the riometer
293 absorption signatures, and compare the resulting estimate of precipitation fluxes with the

294 observed radio wave propagation conditions between the Australian transmitter, NWC, and
295 Casey. Previously Clilverd et al. [2008] used the LANL SOPA electron fluxes to investigate
296 non-dispersive injections of substorm-driven precipitation into the atmosphere. In that study EEP
297 fluxes were used to model a substorm on 01 March 2006 which showed 3 dB of riometer
298 absorption at Macquarie Island, and \sim 12 dB amplitude effect on an Australian transmitter, NTS,
299 received at Casey. No phase observations were available at the time. Although not shown in
300 Clilverd et al. [2008], amplitude measurements of NWC were made at Casey for that event and
301 showed a similar decrease to NTS at Casey, i.e., \sim 14 dB amplitude effect of the substorm-driven
302 EEP. The substorm event reported here shows similar peak riometer absorption levels at similar
303 MLT (midnight) compared with the substorm on 01 March 2006, and with similar peak NWC
304 amplitude changes of \sim 9 dB. We note here that the identification of the quiet day curve for the
305 NWC amplitude data at Casey, particularly that part during the nighttime in the winter months, is
306 difficult and uncertain due to the high variability exhibited from day-to-day. However, the NWC
307 quiet day phase variations are more consistent, and thus the identification of EEP effects on the
308 NWC phase at Casey is a more reliable technique, hence the use of NWC phase in the analysis
309 undertaken in this paper.

310 Given similar riometer substorm absorption levels, it seems reasonable to expect the LANL
311 SOPA-based EEP spectrum used in Clilverd et al. [2008] to represent the EEP at the time of the
312 peak riometer absorption conditions in this study. LANL SOPA data are currently unavailable to
313 check this assumption. However, we are able to make use of the THEMIS SST electron channel
314 measurements in order to estimate the EEP spectrum during this event. Figure 6 shows the
315 electron flux from THEMIS E at the start of the second substorm (diamonds, labelled as
316 12:24 UT). Examination of the THEMIS SST data shows that the electron fluxes and spectral
317 gradient remain essentially constant from 12:24-12:30 UT. Thus, although we often refer to the
318 THEMIS data in terms of the 12:24 UT spectrum, it is also applicable to the spectrum when the

319 riometer shows maximum absorption (12:30 UT). Figure 6 also shows the THEMIS electron flux
320 at the peak of the NWC-Casey phase change (triangles, labelled as 12:51 UT). The solid line
321 represents the electron spectrum determined from LANL during the peak of a similar substorm
322 on 01 March 2006 [Clilverd et al., 2008]. The dotted line represents a fit to the 12:51 UT
323 electron spectra. The LANL spectra and the 12:24 UT THEMIS E spectra are very similar, while
324 the 12:51 UT THEMIS E data shows lower flux levels and a slightly harder spectrum. Figure 6
325 confirms the similarity in the substorm characteristics observed by LANL and by THEMIS, and
326 also confirms that there is little change in the electron spectrum as the substorm evolves. We
327 note that the substorm electron precipitation spectrum reported by Rosenberg et al. [1972] was
328 harder than that observed in this paper, although similar peak riometer absorption levels were
329 recorded.

330 Having determined the electron energy spectrum for the peak fluxes during each substorm
331 event, we can now calculate the impact of electron precipitation on riometer absorption and radio
332 wave propagation with different levels of flux. By calculating height-integrated differential
333 absorption using a method described in Thrane [1973], we can estimate the EEP fluxes required
334 to produce the observed substorm-driven riometer absorption for the Macquarie Island riometer
335 at 12:30 UT on 28 May 2010. Figure 7 shows the change of riometer absorption and NWC phase
336 received at Casey as a function of EEP integral flux >30 keV with units of $\text{cm}^{-2} \text{sr}^{-1} \text{s}^{-1}$, using the
337 THEMIS-derived energy spectra from 12:24 UT. A vertical green line represents the EEP flux
338 levels which produce the observed effects on the riometer and NWC-Casey phase. The EEP-
339 driven mesospheric ionization effects on VLF/LF wave propagation are modeled using the Long
340 Wave Propagation Code [LWPC, Ferguson and Snyder, 1990]. LWPC models VLF signal
341 propagation from any point on Earth to any other point. Given electron density profile
342 parameters for the upper boundary conditions, LWPC calculates the expected amplitude and
343 phase of the VLF signal at the reception point. As in Clilverd et al. [2008] we use a simple

344 ionospheric model to describe the balance of electron number density, N_e , in the lower
345 ionosphere, based on that given by Rodger et al. [1998], and further described by Rodger et al.
346 [2007a]. The electron number density profiles determined using the simple ionospheric electron
347 model for varying precipitation flux magnitudes (30 keV-2.5 MeV) are used as input to the
348 LWPC subionospheric propagation model. Consistent with the work of Berkey et al. [1974] the
349 EEP-affected profiles are applied on only a portion of the transmitter-receiver great circle path
350 between $L=5.2$ and $L=8.9$, thus modeling the effect of precipitation on the NWC phase received
351 at Casey. The effects of the EEP are compared with undisturbed LWPC model phase values for
352 the path using the Thomson et al. [2007] nighttime model ionosphere. A more detailed
353 description of this technique can be found in Clilverd et al. [2008].

354 Throughout this study we assume that the EEP fluxes and spectra are the same over the whole
355 L-shell range affected by the EEP. The substorm L-shell range is based on the average EEP
356 range presented in Berkey et al. [1974], with fine tuning provided by the inter-comparison
357 between riometer absorption observations and the NWC-Casey phase change. Future challenges
358 for this work will be to include L-shell variations in spectra (e.g., Liu et al. [2009b]), and L-shell
359 variations in flux.

360 The results shown in Figure 7 indicate the integral >30 keV flux levels required to generate the
361 observed maximum effects on riometer and radiowave data at 12:30 UT during the second
362 substorm. Both riometer absorption and NWC phase show well ordered responses to increased
363 EEP fluxes. This is in contrast to radio wave amplitude responses where an observed amplitude
364 value could have more than one EEP flux solution (see Figure 5 in Clilverd et al. [2008], and
365 Figure 7 in Rodger et al. [2007c]). Thus the phase analysis performed here allows a clearer
366 identification of the incident EEP flux during the substorm, with less likelihood of a non-unique
367 solution. Figure 7 also confirms that the EEP spectrum used is able to produce both the observed
368 riometer absorption levels, and the observed NWC-Casey phase change using the same EEP flux

369 value, assuming a realistic L -shell range over which the EEP was applied to the NWC-Casey
370 propagation path (about $5 < L < 9$). The modeling indicates that the same EEP also reproduces the
371 peak NWC-Casey amplitude change. The EEP flux level identified by the vertical green line
372 (>30 keV 5.6×10^7 el.cm⁻² sr⁻¹ s⁻¹) is 80% of the LANL SOPA peak substorm integrated flux of
373 01 March 2006 reported in Clilverd et al. [2008].

374 The first substorm produced 0.6 dB of riometer absorption and 100° of phase change on
375 NWC-Casey. Using the results shown in Figure 7 we can determine that the EEP flux level of
376 >30 keV 2×10^6 el.cm⁻² sr⁻¹ s⁻¹ (an integrated energy flux of 1.4 ergs cm⁻² sr⁻¹ s⁻¹) is required to
377 reproduce the riometer absorption. However, assuming a precipitation region that covers $5 < L < 9$,
378 as shown in Figure 7, we would expect 150° of phase change on the NWC-Casey propagation
379 path. The smaller phase change observed therefore suggests that the injection region of the first
380 substorm precipitation region is either latitudinally smaller than the second substorm, or the
381 NWC-Casey response seen at the time of the substorm is not associated with substorm EEP.

382

383 **4.2. Time evolution of the EEP**

384 Here we investigate the time evolution of the second activation event where the riometer
385 absorption peaks at a different time to the peak Casey phase change. Figure 8 shows the second
386 substorm event in detail for NWC-Casey phase change (upper panel), and for the Macquarie
387 Island riometer absorption (lower panel). The vertical dot-dashed line in each panel indicates the
388 time of the onset of the substorm, while two vertical dotted lines indicate (a) the timing of the
389 peak in riometer absorption at 12:30 UT and (b) the timing of the peak in Casey phase change at
390 12:51 UT. In section 4.1 we successfully modelled the former; that is, the riometer absorption
391 and phase response observed at Casey at the same time, i.e., time (a). However, the increase in
392 NWC-Casey phase change at (b) relative to (a) suggests that the NWC-Casey propagation path is
393 experiencing more ionization at this time, although conversely, the reduction in the riometer

394 absorption suggests less ionisation. These changes are consistent either with a change in EEP
395 spectral gradient to higher energies (away from the energies that riometers are sensitive to, i.e.,
396 ~30 keV electrons) or an increase in the proportion of the NWC-Casey propagation path that is
397 experiencing EEP. In Figure 6 we showed that the THEMIS electron spectrum changed only a
398 small amount as the substorm evolved from (a) to (b), and similar calculations to those
399 undertaken in section 4.1 suggest that the small change in spectrum observed could not explain
400 the relative changes in phase or absorption. Thus we conclude that the spectrum remains
401 relatively unchanged, and that the proportion of the NWC-Casey propagation path experiencing
402 EEP has increased.

403 Berkey et al. [1974] observed an expansion poleward and equatorward of the precipitation
404 initiation region shortly after the substorm began. Using an extended precipitation region, the
405 THEMIS spectrum taken at 12:51 UT, we were able to reproduce both the NWC phase change
406 and the riometer absorption values at (b). The expanded precipitation region required is
407 $4.2 < L < 12.6$, and the reduced fluxes of >30 keV were 7.8×10^6 el.cm⁻² sr⁻¹ s⁻¹ (an integrated
408 energy flux of 0.2 ergs cm⁻² sr⁻¹ s⁻¹). This is consistent with the observations of Berkey et al.
409 [1974] which gave $4 < L < 12$. We note here that the riometer absorption data allows us to
410 determine the change in flux in this case, as Macquarie Island remains under the region of
411 precipitation at all times during the substorm.

412

413 **4.3. Substorm EEP eastwards of the injection region**

414 So far we have considered the substorm-driven EEP affects on the Macquarie Island riometer
415 and the NWC transmitter signal received at Casey and Scott Base. From Figure 1 it is apparent
416 that the NWC signals cross under the $L=6$ contour west of Macquarie Island. However, the
417 region of electron precipitation is expected to expand eastwards at the approximate drift velocity
418 of electrons with energies of 50-300 keV [Berkey et al., 1974]. Figure 1 indicates that the NPM,

419 Hawaii, signals have paths that cut the $L=6$ contour close to Macquarie Island (154° longitude,
420 NPM to Casey) and east of Macquarie Island (186° longitude, NPM to Scott Base), so we might
421 expect to see delayed substorm effects particularly on the eastern-most path. We plot the NPM
422 phase change from Scott Base and Casey in Figure 9. The format is similar to previous plots,
423 with the vertical dashed lines representing the two substorm activation times at 11:36 UT and
424 12:20 UT. It is clear that the peak phase change for the two substorms occurs at different times at
425 the two receiver sites, with NPM-Scott Base being delayed by 20 minutes for the first substorm,
426 and 42 minutes for the second substorm. The NPM-Casey substorm signatures show a delay of
427 ~ 5 minutes for the first substorm and no delay for the second substorm. Hence, taking into
428 account the eastward expansion of the EEP, and the timing of substorm signatures in all the
429 datasets, we estimate that the initial EEP injection spans the region $130\text{-}150^\circ\text{E}$ for the first
430 substorm, and $110\text{-}150^\circ\text{E}$ for the second substorm.

431 Using expressions from Walt [1994] we find that the azimuthal drift period around the Earth
432 for electrons at $L=6$ with a pitch angle of 90 degrees, i.e., equatorially trapped, of 50 keV
433 electrons is 154 minutes. For 300 keV electrons it is 30 minutes. The NPM-Scott Base path cuts
434 the $L=6$ contour at 186°E . Thus 50 keV electrons would take 15-34 minutes to travel to this
435 longitude from the extended injection region, which is consistent with the 20 and 42 minute
436 delays observed for the first and second substorms respectively. Further, higher energy electrons
437 such as 300 keV would drift from the injection region to 186°E in 2.5-7 minutes, so we would
438 expect the phase response of NPM at Scott Base to start to respond soon after the substorm
439 activation, and then increase gradually as high fluxes of lower energy electrons arrived. This is
440 what is seen in the experimental observations. The lowest energy electrons that are likely to
441 influence the VLF transmitter propagation at night is ~ 50 keV. Electrons with energies < 50 keV
442 will produce excess ionization at altitudes above the bottom of the D-region [Turunen et al.,
443 2009] and hence the VLF signals propagating at grazing incidence will be insensitive to the

444 excess ionization. Consequently, the delay of the peak of the phase change will be due to the
445 timing of the highest fluxes of >50 keV electrons, which will be when the ~50 keV electron
446 precipitation has had time to drift around to 186°E longitude.

447

448 **4.4. The unexplained NWC-Scott Base phase changes**

449 The upper panel of Figure 5 shows the NWC-Casey phase change during the substorm period.
450 The NWC-Scott Base phase change is shown in the middle panel, and although there is a strong
451 similarity in the phase change patterns, there appears to be a time shift between the two by 20
452 minutes with NWC-Scott Base leading NWC-Casey. This suggests that the phase change on the
453 NWC-Scott Base propagation path is driven in a similar way to NWC-Casey, but 20 minutes
454 earlier. This result can only be explained if the NWC-Scott Base phase effects are due to the EEP
455 from the first substorm (and hence correspond to a delay of ~34 minutes) whilst the NWC-Casey
456 phase effect must be due to the second substorm. We note here that the instrument timing at
457 Casey and Scott Base are accurate to <1 s, and that there is no offset between them.

458 We separate the peak phase changes associated with substorm 1 and substorm 2 and show
459 them in two panels in Figure 10. The plot shows the phase changes observed during substorm 1
460 (upper panel) and substorm 2 (lower panel) expressed as a percentage, where 100% is defined as
461 the maximum phase change caused by the initial substorm injections on each individual
462 propagation path, and not the phase change associated with the latitudinal expansion which
463 follows. The longitude of each propagation path where it cuts the $L=6$ contour (indicated in
464 Figure 1) is provided as a label, e.g., 112°E (NWC-Casey), 123°E (NWC-Scott Base), 154°E
465 (NPM-Casey), 186°E (NPM-Scott Base), 200°E (NLK-Scott Base). Substorm 1 shows an
466 increasing delay of the peak phase effect with eastwards longitude – particularly shown by
467 NPM-Scott Base and NLK-Scott Base. Typically we observe drifts of 35-40° eastwards in ~20
468 minutes. This corresponds to a drift period of 180 mins, which is equivalent to the drift period of

469 ~40 keV electrons at $L=6$. We note that all longitudes show an almost immediate phase increase
470 response to the substorm injection, exhibiting delays of <3 mins for $\sim 40^\circ$ of longitude drift and
471 therefore evidence of the injection of electron energies of ~ 1 MeV.

472 In substorm 2 we find that the paths with $L=6$ crossing points at longitudes of 112°E (NWC-
473 Casey) and 154°E (NPM-Casey) react at about the same time, suggesting an injection region
474 somewhere in between the two longitudes, while 186°E (NPM-Scott Base) shows a peak phase
475 effect with a delay of 40 mins that suggests a drift period of ~ 400 mins, and therefore electron
476 energies of ~ 20 keV. This suggests that electron precipitation is occurring involving lower
477 energies in the second substorm compared with the first – hence the longer drift delays observed.

478 In the first substorm Figure 10 shows that the western-most path (123°E , NPM-Casey) reaches
479 its peak phase change later than all of the other paths plotted. This is consistent with Berkey et
480 al. [1974] who showed that despite the general picture of eastwards electron drift dominating,
481 there can be some westwards expansion of the precipitation region that is usually slower than the
482 eastwards drift rate, and which may be associated with the westward travelling surge in the
483 visual aurora.

484 Given the understanding of the generally eastwards progression in the peak phase changes in
485 Figure 10 we can see that the first substorm initially does not show the latitudinal expansion in
486 the precipitation region to $4 < L < 12$ as discussed earlier in the paper, i.e., no obvious L -shell
487 expansion identified on the 154°E and 186°E longitudes. The eastern-most path (NLK-Scott
488 Base at $\sim 200^\circ\text{E}$) shows evidence of this happening, as well as the western-most path NWC-Scott
489 Base (123°E), significantly later on. This indicates that, as far as the VLF observations are
490 concerned, the L -shell expansion occurs ~ 40 minutes after the initial injection, both to the east
491 and to the west of the injection region. Further modeling of the time variation of the EEP fluxes,
492 and L -shell coverage will be undertaken in a future study.

493 For the second substorm the latitudinal expansion happens on NWC-Casey at $\sim 112^\circ\text{E}$ with the
494 shortest delay time we observed of 30 minutes, and on NPM-Scott Base at $\sim 186^\circ\text{E}$ much later on
495 at ~ 70 minutes. As in the first substorm, the path in between (154°E) shows a much weaker L -
496 shell expansion signature. This suggests that the second substorm is more dynamic in its
497 expansion westwards than the first. Thus we conclude that although both substorms occurred at
498 similar local times, with EEP injections into the same geographical region, there are significant
499 differences in behavior between the two. To the east of the initial injection region the timing of
500 the latitudinal expansion appears to be a function of the longitudinal expansion rate, and there is
501 nearly a factor of two difference between the two substorms. To the west, the relationship
502 between latitudinal and longitudinal expansion appears reversed compared with the east.

503

504 **5. Summary**

505 In this study we examine energetic electron precipitation characteristics from two substorm
506 precipitation events on 28 May 2010. The substorms occurred near MLT midnight in the New
507 Zealand/Australia sector, with signatures observed from 11:36 UT until $\sim 13:30$ UT. We present
508 AARDDVARK ground-based radio wave phase observations from NWC, Australia, NPM,
509 Hawaii, and NLK, Seattle, received at Casey, Antarctica (66.3°S , 110.5°E , $L > 999$) and Scott
510 Base, Antarctica (77.8°S , 166.8°E , $L > 32$). We also include the Macquarie Island riometer
511 absorption data (54.5°S , 158.9°E , $L = 5.4$), and THEMIS E Solid State Telescope (SST)
512 observations. All three instruments observed substorm signatures during the substorm events,
513 consistent with their co-location in the longitudes of Australia. The THEMIS E magnetic field
514 components showed clear signatures of dipolarization at the times of both substorm activations.

515 It was possible to accurately reproduce the peak observed riometer absorption at Macquarie
516 Island (3.2 dB, $L = 5.4$), and the associated NWC radio wave phase change observed at Casey,
517 Antarctica (208°). We used an electron precipitation spectrum taken from THEMIS E electron

518 flux measurements, which was consistent with the LANL-97A energetic electron flux
519 measurements from a similar substorm studied by Clilverd et al. [2008]. Our calculations were
520 based on modeling the impact of energetic electron precipitation in a region covering $5 < L < 9$.
521 This is consistent with the concept that the electron precipitation injection region is restricted to
522 near-geosynchronous orbit L -shells. The flux levels required of >30 keV 5.6×10^7 el.cm⁻² sr⁻¹ s⁻¹
523 (an integrated energy flux of 1.4 ergs cm⁻² sr⁻¹ s⁻¹) were 80% of the peak fluxes observed in a
524 similar substorm by LANL-97A in 2007 by Clilverd et al. [2008].

525 The largest phase change seen at Casey showed a double peaked structure, initially at
526 12:30 UT with peak values of $\sim 208^\circ$, eventually maximising at 12:51 UT with phase change
527 values of 265° . Using an extended precipitation region after the initial injection consistent with
528 Berkey et al. [1974], the THEMIS electron spectrum taken at 12:51 UT, we were able to
529 reproduce both the NWC phase change and associated riometer absorption values of 1.2 dB.
530 The extended precipitation region was $4.2 < L < 12.6$, and the >30 keV flux was 7.8×10^6 el.cm⁻²
531 sr⁻¹ s⁻¹ (an integrated energy flux of 0.2 ergs cm⁻² sr⁻¹ s⁻¹). Thus we show that by using a single
532 riometer site in combination with a single AARDDVARK radio wave receiver site we are in
533 principle able to describe the evolution of the substorm precipitation flux and the latitudinal
534 expansion of the substorm region.

535 In this study of a pair of substorm events we conclude that although both substorms occurred
536 at similar local times, with EEP injections into approximately the same geographical region, the
537 first substorm involved less EEP flux, but the precipitation region drifted eastwards more
538 quickly than the second, larger, event. This study has shown that it is possible to successfully
539 combine AARDDVARK radio wave observations, THEMIS satellite measurements, and
540 riometer absorption data in order to investigate the characteristics of substorm-induced
541 energetic electron precipitation in detail.

542

543 **Acknowledgments.** The authors would like to acknowledge the support of the Australian
544 Antarctic Division project number: ASAC 1324 for the Casey data, and in particular the
545 assistance of Ian Phillips. We would also like to acknowledge the use of the AAD data system
546 for the provision of the Macquarie Island Riometer data,
547 http://www.ips.gov.au/World_Data_Centre/1/8. The Scott Base experiment is supported by
548 Antarctica New Zealand, event number K060. We acknowledge NASA contract NAS5-02099
549 and V. Angelououlos for the use of data from the THEMIS Mission. Specifically: D. Larson and
550 R.P. Lin for use of the SST data. IJR is funded by the Canadian Space Agency.
551 The research leading to these results has received funding from the European Union Seventh
552 Framework Programme [FP7/2007-2013] under grant agreement n°263218.

553

554

555

556 **References**

557 Akasofu, S.-I. (1964), The development of the auroral substorm, *Planet. Space. Sci.*, 12, 273-
558 282, doi: 10.1016/0032-0633(64)90151-5.

559

560 Angelopoulos, V. (2008), The THEMIS mission, *Space Sci. Rev.*, 141, 5-34, doi:
561 10.1007/s11214-008-9336-1.

562

563 Axford, W. (1999), Reconnection, substorms and solar flares, *Physics and Chemistry of the*
564 *Earth C*, 24, 147-151, doi: 10.1016/S1464-1917(98)00022-1.

565

566 Baker, D. N., W. Aiello, J. R. Asbridge, R. D. Belian, P. R. Higbie, R. W. Klebesadel, J. G.
567 Laros and E. R. Tech (1985), "Los Alamos Energetic Particle Sensor Systems at
568 Geostationary Orbit," AIAA 85-0243.

569

570 Bailey, D. K. (1968), Some quantitative aspects of electron precipitation in and near the auroral
571 zone, *Rev. Geophys.*, 6, 289- 346.

572

573 Barr, R., D. L. Jones, and C. J. Rodger (2000), ELF and VLF radio waves, *J. Atmos. Sol.-Terr.*
574 *Phys.*, 62, 1689-1718.

575

576 Berkey, F. T., V. M. Driatskiy, K. Henriksen, B. Hultqvist, D. H. Jelly, T. I. Shchuka, A.
577 Theander, and J. Yliniemi (1974), A synoptic investigation of particle precipitation dynamics
578 for 60 substorms in IQSY (1964–1965) and IASY (1969), *Planet. Space Sci.*, 22, 255–307.
579

580 Brasseur, G., and S. Solomon (2005), *Aeronomy of the Middle Atmosphere*, third ed., D. Reidel
581 Publishing Company, Dordrecht.
582

583 Clilverd, M. A., C. J. Rodger, J. B. Brundell, N. Cobbett, J. Bähr, T. Moffat-Griffin, A. J.
584 Kavanagh, A. Seppälä, N. R. Thomson, R. H. W. Friedel, and F. W. Menk (2008), Energetic
585 electron precipitation during sub-storm injection events: high latitude fluxes and an
586 unexpected mid-latitude signature, *J. Geophys. Res.*, 113, A10311, doi: 10.1029/
587 2008JA013220.
588

589 Clilverd, M. A., C. J. Rodger, N. R. Thomson, J. B. Brundell, Th. Ulich, J. Lichtenberger, N.
590 Cobbett, A. B. Collier, F. W. Menk, A. Seppälä, P. T. Verronen, and E. Turunen (2009),
591 Remote sensing space weather events: the AARDDVARK network, *Space Weather*, 7,
592 S04001, doi: 10.1029/2008SW000412.
593

594 Clilverd, M. A., C. J. Rodger, R. J. Gamble, Th. Ulich, T. Raita, A. Seppälä, J. C. Green, N. R.
595 Thomson, J.-A. Sauvaud, and M. Parrot (2010), Ground-based estimates of outer radiation belt
596 energetic electron precipitation fluxes into the atmosphere, *J. Geophys. Res.*, 115, A12304,
597 doi: 10.1029/2010JA015638.
598

599 Ferguson, J. A., and F. P. Snyder (1990), Computer programs for assessment of long wavelength
600 radio communications, Tech. Doc. 1773, Natl. Ocean Syst. Cent., San Diego, California.
601

602 Jelly, D., and N. Brice (1967), Changes in the Van Allen radiation associated with polar
603 substorms, *J. Geophys. Res.*, 72, 5919- 5931.
604

605 Kavanagh, A. J., G. Lu, E. F. Donovan, G.D. Reeves, F. Honary, J. Manninen, T. J. Immel
606 (2007), Energetic electron precipitation during sawtooth injections. *Ann. Geophys.*, 25, 1199-
607 1214.
608

609 Little, C.G. and H. Leinbach (1959), The riometer: a device for the continuous measurements of
610 ionospheric absorption, *Proc. IRE*, 37, 315-320.
611

612 Liu, J., et al. (2009a), THEMIS observation of a substorm event on 04:35, 22 February 2008,
613 *Ann. Geophys.*, 27, 1831-1841.
614

615 Liu, J., et al. (2009b), Observations and modeling of the injection observed by THEMIS and
616 LANL satellites during the 23 March 2007 substorm event, *J. Geophys. Res.*, 114, A00C18,
617 doi: 10.1029/2008JA013498.
618

619 Lopez, R.E., and A.T.Y. Liu (1990), A multisatellite case study of the expansion of a substorm
620 current wedge in the near-earth magnetotail, *J. Geophys. Res.*, 95, 8009-8017.
621

622 Lorentzen, K. R., J. B. Blake, U. S. Inan, J. Bortnik (2001), Observations of relativistic electron
623 microbursts in association with VLF chorus, *J. Geophys. Res.* Vol. 106, 6017-6027.
624

625 Millan, R. M., R. P. Lin, D. M. Smith, K. R. Lorentzen, and M. P. McCarthy (2002), X-ray
626 observations of MeV electron precipitation with a balloon-borne germanium spectrometer,
627 *Geophys. Res. Lett.*, 29(24), 2194, doi: 10.1029/2002GL015922.

628

629 Nagai, T. et al. (1998), Structure and dynamics of magnetic reconnection for substorm onsets
630 with Geotail observations, *J. Geophys. Res.*, 103, 4419-4440, doi: 10.1029/97JA02190.

631

632 Randall, C. E., et al. (2005), Stratospheric effects of energetic particle precipitation in 2003–
633 2004, *Geophys. Res. Lett.*, 32, L05802, doi:10.1029/2004GL022003.

634

635 Reeves, G, A Chan, and C J Rodger (2009), New Directions for Radiation Belt Research, *Space*
636 *Weather*, 7(7), S07004, doi: 10.1029/2008SW000436.

637

638 Rodger, C. J., O. A. Molchanov, and N. R. Thomson (1998), Relaxation of transient ionization in
639 the lower ionosphere, *J. Geophys. Res.*, 103(4), 6969-6975.

640

641 Rodger, C. J., M. A. Clilverd, N. R. Thomson, R. J. Gamble, A. Seppälä, E. Turunen, N. P.
642 Meredith, M. Parrot, J. A. Sauvaud, and J.-J. Berthelier (2007a), Radiation belt electron
643 precipitation into the atmosphere: recovery from a geomagnetic storm, *J. Geophys. Res.*, 112,
644 A11307, doi: 10.1029/2007JA012383.

645

646 Rodger, C. J., M. A. Clilverd, D. Nunn, P. T. Verronen, J. Bortnik, E. Turunen (2007b), Storm
647 time, short-lived bursts of relativistic electron precipitation detected by subionospheric radio
648 wave propagation, *J. Geophys. Res.*, 112, A07301, doi: 10.1029/2007JA012347.

649

650 Rodger, C. J., M. A. Clilverd, N. R. Thomson, R. J. Gamble, A. Seppälä, E. Turunen, N. P.
651 Meredith, M. Parrot, J. A. Sauvaud, and J.-J. Berthelier (2007c), Radiation belt electron
652 precipitation into the atmosphere: recovery from a geomagnetic storm, *J. Geophys. Res.*, 112,
653 A11307, doi: 10.1029/2007JA012383.

654

655 Rodger, C. J., T. Raita, M. A. Clilverd, A. Seppälä, S. Dietrich, N. R. Thomson, and Th. Ulich
656 (2008), Observations of relativistic electron precipitation from the radiation belts driven by
657 EMIC Waves, *Geophys. Res. Lett.*, 35, L16106, doi: 10.1029/2008GL034804.

658

659 Rodger, C. J., M. A. Clilverd, J. Green, and M.-M. Lam (2010a), Use of POES SEM-2
660 observations to examine radiation belt dynamics and energetic electron precipitation in to the
661 atmosphere, *J. Geophys. Res.*, 115, A04202, doi: 10.1029/ 2008JA014023.

662

663 Rodger, C. J., M. A. Clilverd, A. Seppälä, N. R. Thomson, R. J. Gamble, M. Parrot, J.-A.
664 Sauvaud and Th. Ulich (2010b), Radiation belt electron precipitation due to geomagnetic
665 storms: significance to middle atmosphere ozone chemistry, *J. Geophys. Res.*, 115, A11320,
666 doi: 10.1029/2010JA015599.

667

668 Rosenberg, T. J., L. J. Lanzerotti, D. K. Bailey, and J. D. Pierson (1972), Energy spectra in
669 relativistic electron precipitation events, *J. Atmos. Terr. Phys.*, 34, 1977-1990.

670

671 Sandholt, P. E., et al. (2002), Multistage substorm expansion: Auroral dynamics in relation to
672 plasma sheet particle injection, precipitation, and plasma convection, *J. Geophys. Res.*, 107,
673 1342, doi: 10.1029/2001JA900116.

674
675 Seppälä, A, M. A. Clilverd, and C. J. Rodger (2007), NO_x enhancements in the middle
676 atmosphere during 2003-2004 polar winter: Relative significance of solar proton events and
677 the aurora as a source, *J. Geophys. Res.*, D23303, doi: 10.1029/2006JD008326.
678
679 Seppälä, A., C. E. Randall, M. A. Clilverd, E. Rozanov, and C. J. Rodger (2009), Geomagnetic
680 activity and polar surface level air temperature variability, *J. Geophys. Res.*, 114, A10312, doi:
681 10.1029/2008JA014029.
682
683 Spanswick, E., E. Donovan, R. Friedel, and A. Korth (2007), Ground based identification of
684 dispersionless electron injections, *Geophys. Res. Lett.*, 34, L03101, doi:
685 10.1029/2006GL028329.
686
687 Spanswick, E., et al. (2009), Global observations of substorm injection region evolution: 27
688 August 2001, *Ann. Geophys.*, 27, 2019-2025.
689
690 Thomson, N. R., M. A. Clilverd, and W. M. McRae (2007), Nighttime ionospheric D region
691 parameters from VLF phase and amplitude, *J. Geophys. Res.*, 112, A07304, doi:
692 10.1029/2007JA012271.
693
694 Thorne, R. M., and T. R. Larsen (1976), An investigation of relativistic electron precipitation
695 events and their association with magnetic substorm activity, *J. Geophys. Res.*, 81, 5501-
696 5506.
697
698 Thrane, E. V. (1973), RadioWave Propagation, which is from the book Egeland, A., O. Holter,
699 and A. Omholt (Eds.), *Cosmical Geophysics*, Universitetsforlaget, 18, 267-281.
700
701 Turunen, E., P. T. Verronen, A. Seppälä, C. J. Rodger, M. A. Clilverd, J. Tamminen, C. F. Enell
702 and Th. Ulich (2009), Impact of different precipitation energies on NO_x generation during
703 geomagnetic storms, *J. Atmos. Sol.-Terr. Phys.*, 71, pp. 1176-1189,
704 doi:10.1016/j.jastp.2008.07.005.
705
706 Verronen, P. T., C. J. Rodger, M. A. Clilverd, and S. Wang (2011), First evidence of
707 mesospheric hydroxyl response to electron precipitation from the radiation belts, *J. Geophys.*
708 *Res.*, 116, D07307, doi: 10.1029/2010JD014965.
709
710 Walt, M. (1994), *Introduction to Geomagnetically Trapped Radiation*, Cambridge Atmospheric
711 and Space Series, Cambridge Univ. Press, pp 49.
712
713
714
715
716 M. A. Clilverd, and N. Cobbett, British Antarctic Survey (NERC), High Cross, Madingley Road, Cambridge CB3 0ET, England,
717 U.K. (email: macl@bas.ac.uk, nco@bas.ac.uk)
718
719 F. W. Menk, School of Mathematical and Physical Sciences and Cooperative Research Centre for Satellite Systems, University
720 of Newcastle, Callaghan, N.S.W., 2308, Australia. (email: fred.menk@newcastle.edu.au)
721
722 I. J. Rae, Department of Physics, University of Alberta, Edmonton, AB T6G 0A1, Canada. (email: Jonathan.Rae@ualberta.ca)
723
724 J. Brundell, C. J. Rodger, and N. R. Thomson, Department of Physics, University of Otago, P.O. Box 56, Dunedin, New Zealand.
725 (email: james@brundell.co.nz, crodger@physics.otago.ac.nz, n_thomson@physics.otago.ac.nz)

726
727
728
729

P. T. Verronen, Earth Observation, Finnish Meteorological Institute, P.O. Box 503, FI-00101 Helsinki, Finland
(email: Pekka.verronen@fmi.fi)

730 (Received N x, 2011; N x 27, 2011;

731 accepted N x, 2011.)

732

733 CLILVERD ET AL.: SUBSTORM ELECTRON PRECIPITATION

734

735 **Figures**

736 **Figure 1.** A map of the subionospheric VLF propagation paths from the NWC
737 (green circle), NPM, and NLK transmitters to the Casey and Scott Base receivers in
738 Antarctica (red diamonds). Contours of constant L -shell are shown for $L=4$, 6, and 12
739 (blue lines). The locations of the southern hemisphere footprint of THEMIS E during
740 the substorm events studied in this paper (red line), and Macquarie Island (solid
741 square) are also indicated.

742 **Figure 2.** Upper panel. The variation of nighttime phase from NWC to Casey on
743 three typical event days in 2009-2010. The days have been offset to aid presentation.
744 The normal quiet day behavior is shown by dotted lines. Electron precipitation events
745 are observed as increases in phase, followed by a slow recovery to the quiet day
746 levels. Phase decreases occur at sunset (~05-10 UT) and phase increases occur at
747 sunrise (~21-24 UT). Lower panel. Same as above but for NWC received at Scott
748 Base.

749 **Figure 3.** The background conditions for the 28 May 2010 precipitation event.
750 Panels show the variation of solar wind speed, Dst, Kp, and GOES >10 MeV proton
751 fluence for 27 – 29 May 2010. The 28 May precipitation event occurs after a jump in
752 solar wind speed, during the positive phase of a Dst disturbance, during low-
753 moderate Kp levels, and with no enhancement of solar proton precipitation.

754 **Figure 4.** A summary plot of the THEMIS E SST data on 28 May 2010. Upper
755 panel. The variation in electron energy flux from 10-14 UT observed over a range of
756 energy channels indicated by the coloured labels on the right hand side. **Middle**
757 **panel. The variation of the >30 keV integrated energy flux.** Lower panel. The
758 variation of the magnetic field components **in Geocentric Solar Ecliptic (GSE)**
759 **coordinates** during the same period. Note the reversal of the x (blue line) and z (red

760 line) components as a result of two substorm activations at ~11:36 UT and
761 ~12:20 UT. The position of the satellite at 1000 UT was $[x,y,z]=[-6.7, -7.2, 0.0]$, and
762 at 1400 UT was $[x,y,z]=[-1.2, -5.4, 0.2]$.

763

764 **Figure 5.** Upper panel. The variation of NWC phase received at Casey for 10-16 UT
765 on 28 May 2010. Middle panel: The variation of NWC phase received at Scott Base
766 during the same period. Lower panel. Macquarie Island riometer absorption during
767 the same period. The times of the two substorm activations seen in THEMIS data are
768 indicated by vertical dashed lines.

769 **Figure 6.** THEMIS E electron flux measurements at 12:24 UT (diamonds) and
770 12:51 UT (triangles) on 28 May 2010. The electron energy spectrum observed by
771 LANL and presented in Clilverd et al. [2008] is shown by the solid line. The least
772 squares fit to the 12:51 UT observations is given by the dotted line.

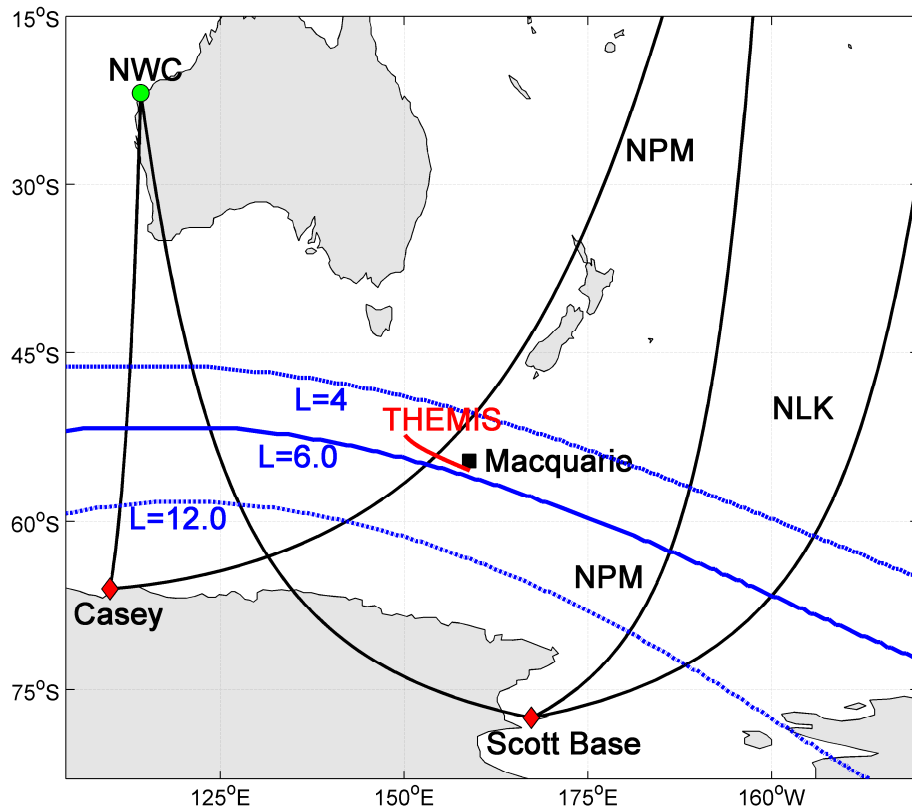
773 **Figure 7.** Upper panel: The calculated NWC phase change as a function of electron
774 precipitation flux >30 keV at Casey. Lower panel: The equivalent riometer
775 absorption level at Macquarie Island. The green vertical line indicates the flux levels
776 required to reproduce the NWC-Casey phase, and riometer absorption values at the
777 peak of the second substorm (values indicated by horizontal grey lines).

778 **Figure 8.** Upper panel. NWC phase change at Casey during second substorm event.
779 Lower panel. Macquarie Island riometer absorption. The vertical dot-dashed line
780 indicates the start of the substorm event as determined by THEMIS E magnetometer
781 dipolarisation timing. The vertical dotted lines labelled (a) and (b) indicate the timing
782 of the peak riometer absorption, and the peak phase change respectively.

783 **Figure 9** The NPM-Scott Base and NPM-Casey phase change on 10-16 UT, 28 May
784 2010. Vertical lines represent the activation times of the two substorms.

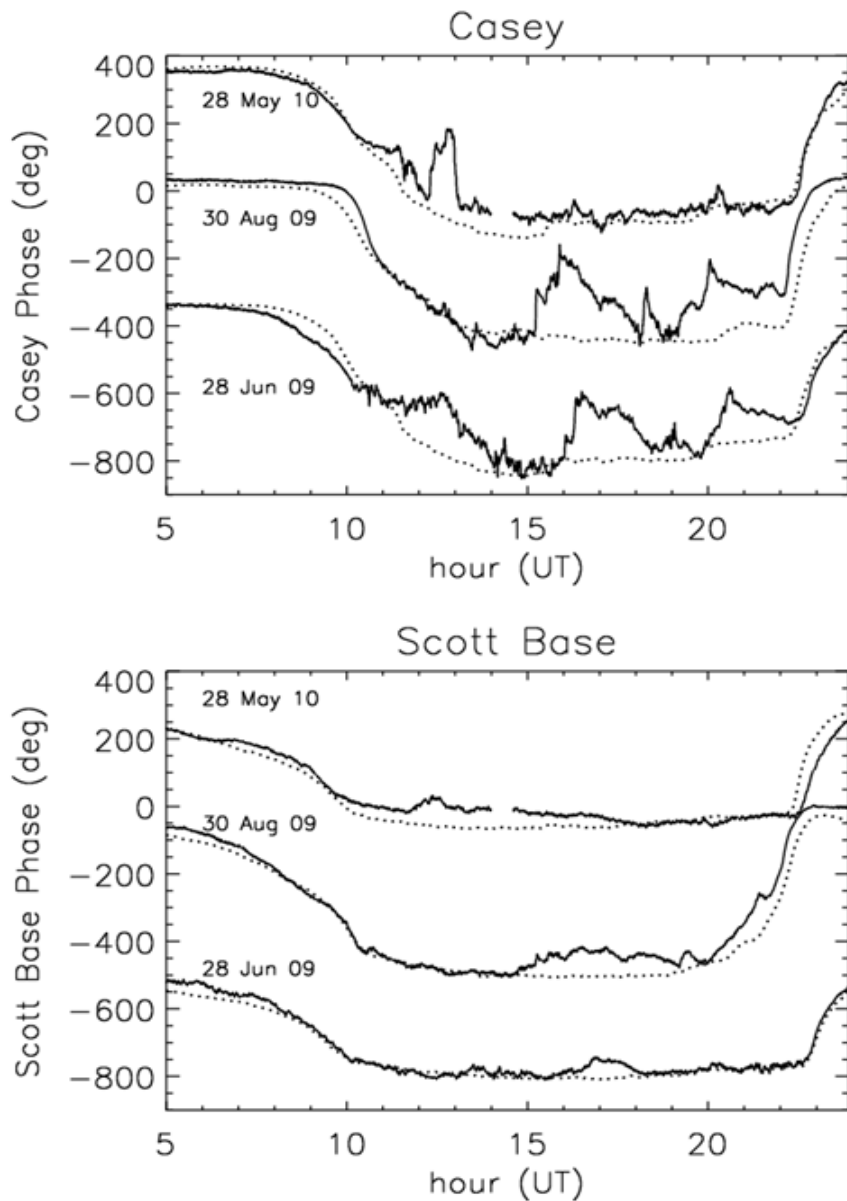
785 **Figure 10.** A summary of the phase changes observed during substorm 1 (upper
786 panel) and substorm 2 (lower panel). The phase change is expressed as a percentage,
787 with 100% defined as the maximum phase change caused by the substorm injections.
788 The longitude of each propagation path where it cuts the $L=6$ contour (as shown in
789 Figure 1) is indicated, e.g., 112°E (NWC-Casey), 123°E (NWC-Scott Base), 154°E
790 (NPM-Casey), 186°E (NPM-Scott Base), 195°E (NLK-Scott Base). The periods of
791 expanding L-shell extent of the substorm-induced EEP are indicated.

792



794

795 **Figure 1.** A map of the subionospheric VLF propagation paths from the NWC
 796 (green circle), NPM, and NLK transmitters to the Casey and Scott Base receivers in
 797 Antarctica (red diamonds). Contours of constant L -shell are shown for $L=4$, 6, and 12
 798 (blue lines). The locations of the southern hemisphere footprint of THEMIS E during
 799 the substorm events studied in this paper (red line), and Macquarie Island (solid
 800 square) are also indicated.



801

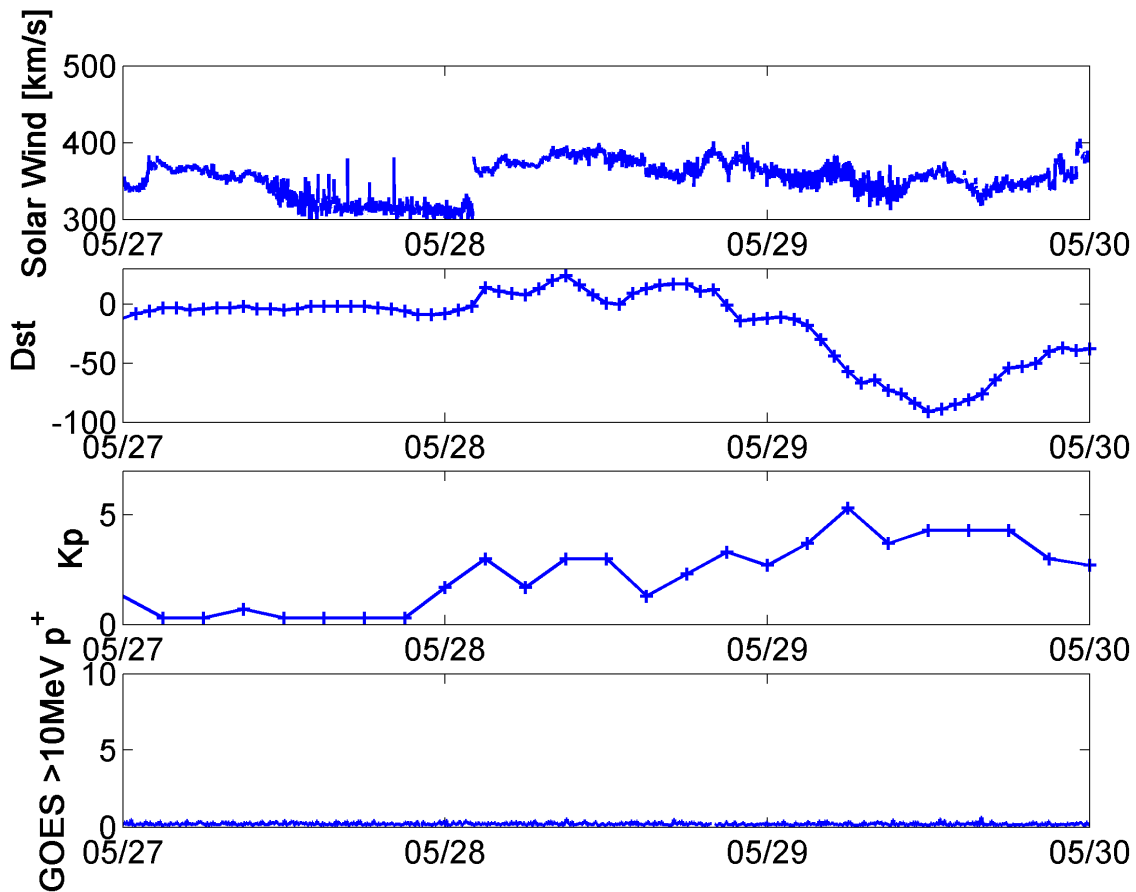
802 **Figure 2.** Upper panel. The variation of nighttime phase from NWC to Casey on
 803 three typical event days in 2009-2010. The days have been offset to aid presentation.

804 The normal quiet day behavior is shown by dotted lines. Electron precipitation events
 805 are observed as increases in phase, followed by a slow recovery to the quiet day
 806 levels. Phase decreases occur at sunset (~05-10 UT) and phase increases occur at

807 sunrise (~21-24 UT). Lower panel. Same as above but for NWC received at Scott

808 Base.

809



810

811 **Figure 3.** The background conditions for the 28 May 2010 precipitation event.

812 Panels show the variation of solar wind speed, Dst, Kp, and GOES >10 MeV proton

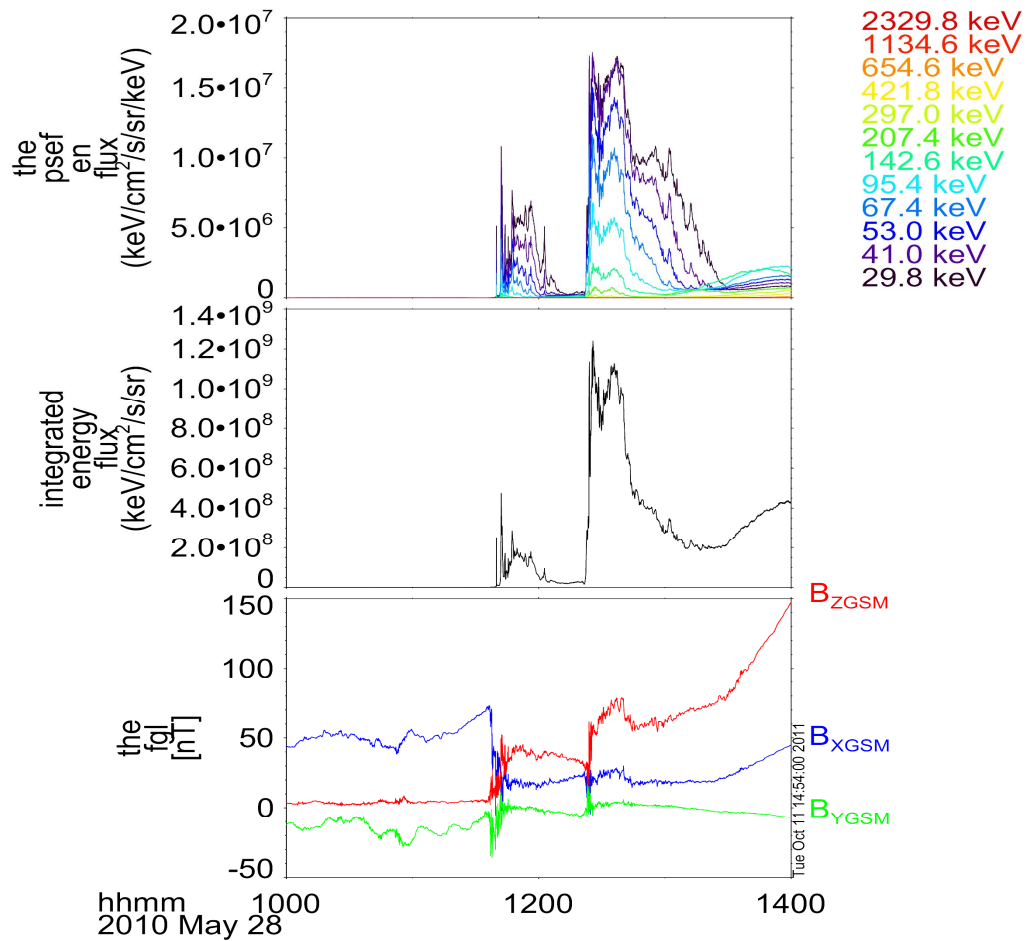
813 fluence for 27 – 29 May 2010. The 28 May precipitation event occurs after a jump in

814 solar wind speed, during the positive phase of a Dst disturbance, during low-

815 moderate Kp levels, and with no enhancement of solar proton precipitation.

816

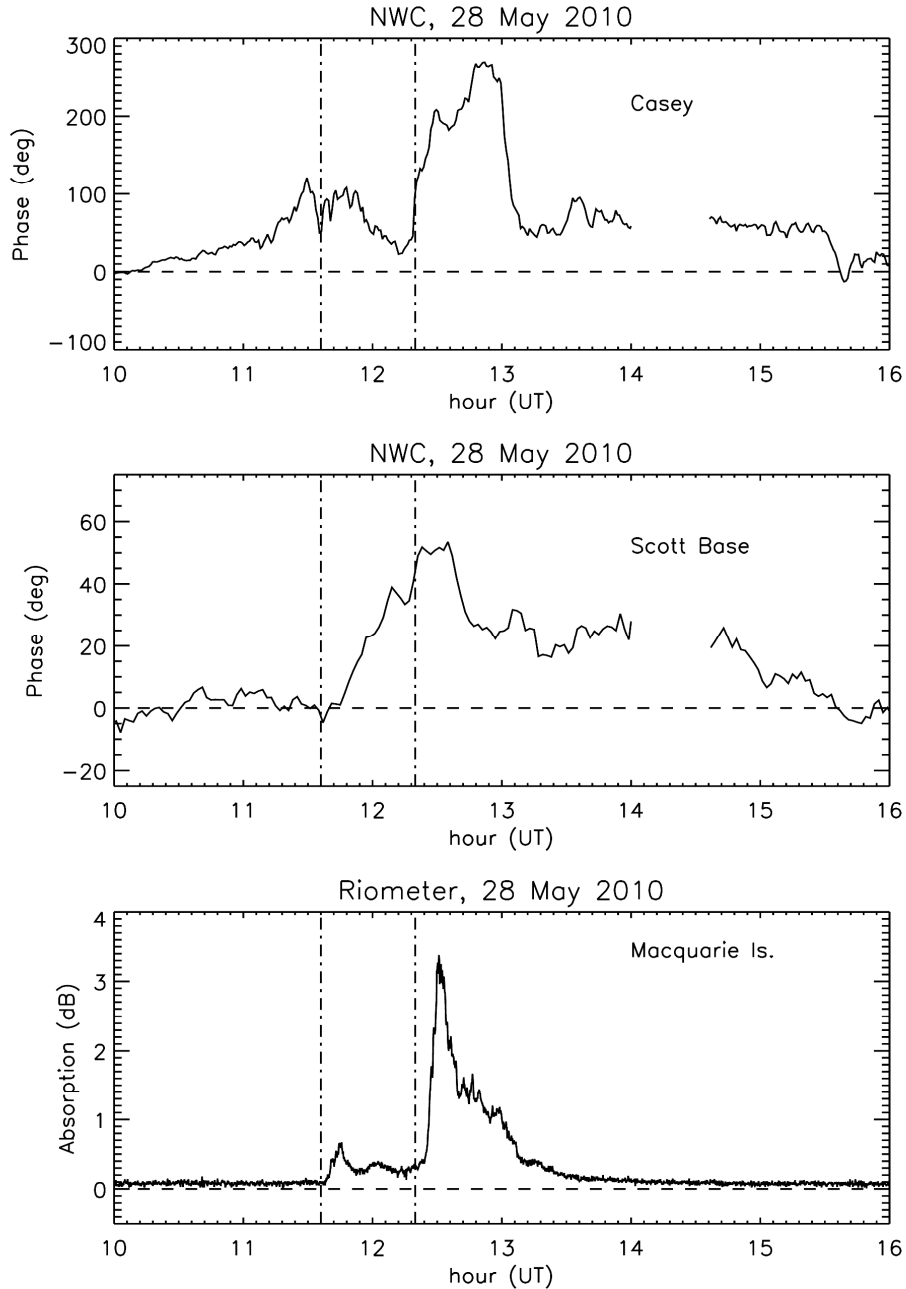
817



819

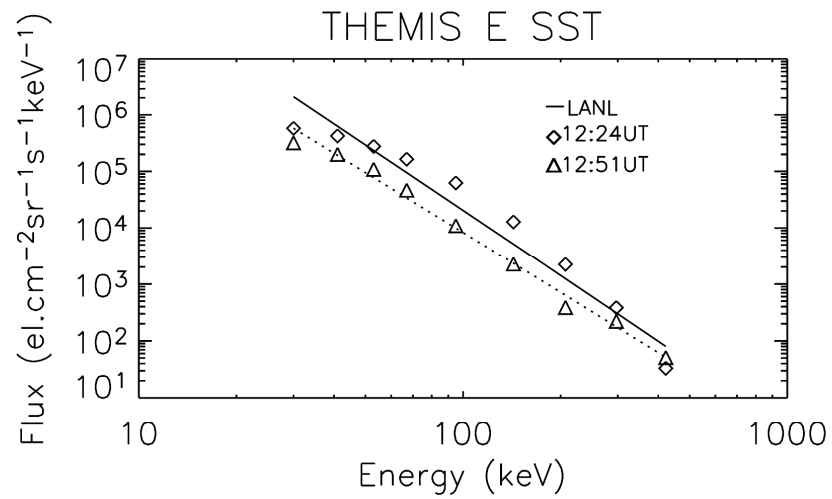
820 **Figure 4.** A summary plot of the THEMIS E SST data on 28 May 2010. Upper
 821 panel. The variation in electron energy flux from 10-14 UT observed over a range of
 822 energy channels indicated by the coloured labels on the right hand side. **Middle**
 823 **panel.** The variation of the >30 keV integrated energy flux. Lower panel. The
 824 variation of the magnetic field components **in Geocentric Solar Ecliptic (GSE)**
 825 **coordinates** during the same period. Note the reversal of the x (blue line) and z (red
 826 line) components as a result of two substorm activations at ~11:36 UT and
 827 ~12:20 UT. **The position of the satellite at 1000 UT was [x,y,z]=[-6.7, -7.2, 0.0], and**
 828 **at 1400 UT was [x,y,z]=[-1.2, -5.4, 0.2].**

829



830

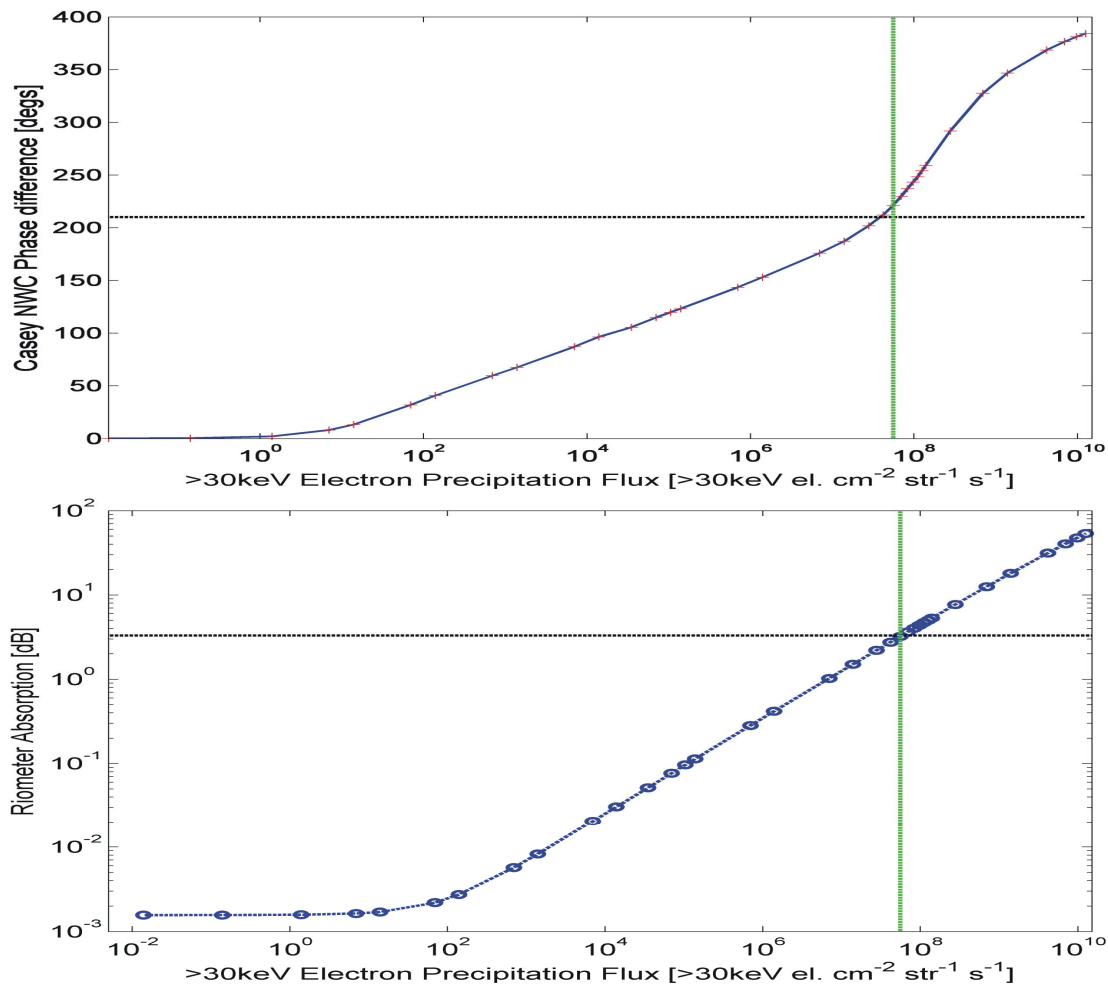
831 **Figure 5.** Upper panel. The variation of NWC phase received at Casey for 10-16 UT
 832 on 28 May 2010. Middle panel: The variation of NWC phase received at Scott Base
 833 during the same period. At 14:04 UT there was a NWC off-air period lasting for ~0.5
 834 hour. Lower panel. Macquarie Island riometer absorption during the same period.
 835 The times of the two substorm activations seen in THEMIS data are indicated by
 836 vertical dashed lines.



838

839 **Figure 6.** THEMIS E electron flux measurements at 12:24 UT (diamonds) and
 840 12:51 UT (triangles) on 28 May 2010. The electron energy spectrum observed by
 841 LANL and presented in Clilverd et al. [2008] is shown by the solid line. The least
 842 squares fit to the 12:51 UT observations is given by the dotted line.

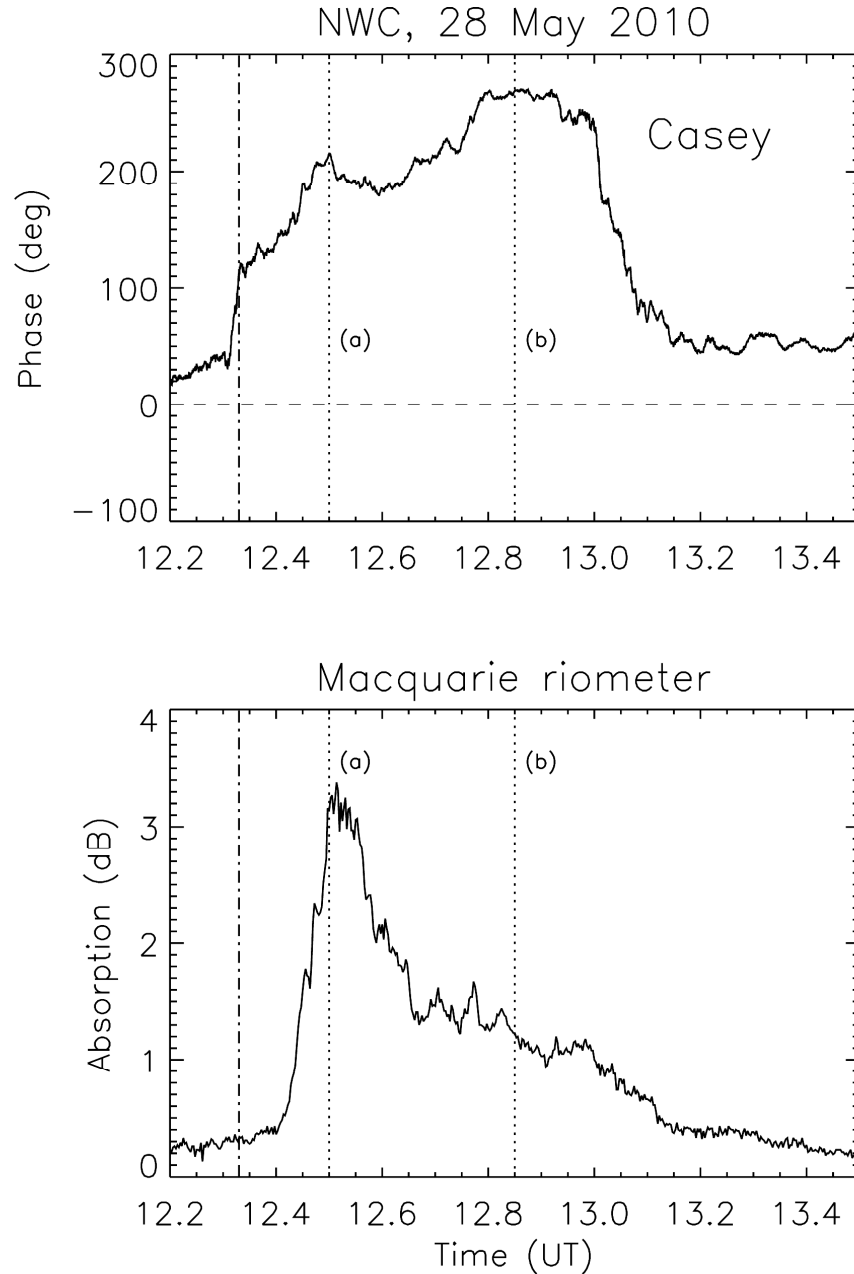
843



844

845 **Figure 7.** Upper panel: The calculated NWC phase change as a function of electron
 846 precipitation flux >30 keV at Casey. Lower panel: The equivalent riometer
 847 absorption level at Macquarie Island. The green vertical line indicates the flux levels
 848 required to reproduce the NWC-Casey phase, and riometer absorption values at the
 849 peak of the second substorm (values indicated by horizontal grey lines).

850



852

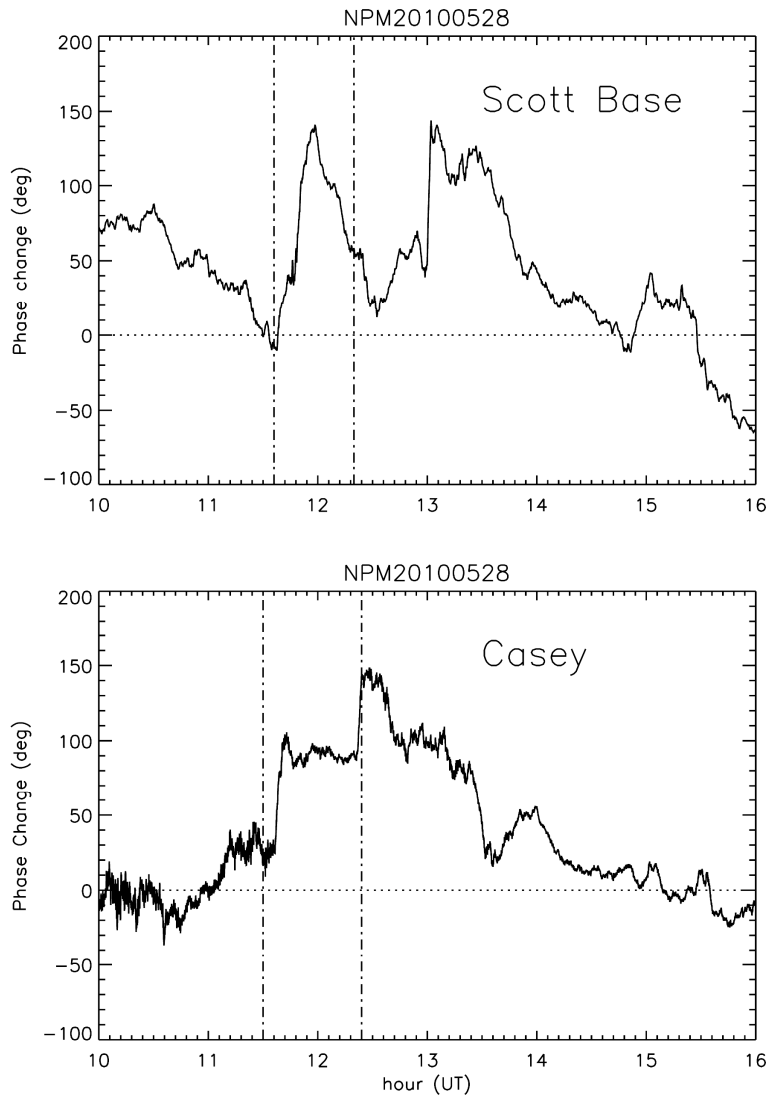
853 **Figure 8.** Upper panel. NWC phase change at Casey during second substorm event.

854 lower panel. Macquarie Island riometer absorption. The vertical dot-dashed line

855 indicates the start of the substorm event as determined by THEMIS E magnetometer

856 dipolarisation timing. The vertical dotted lines labelled (a) and (b) indicate the timing

857 of the peak riometer absorption, and the peak phase change respectively.

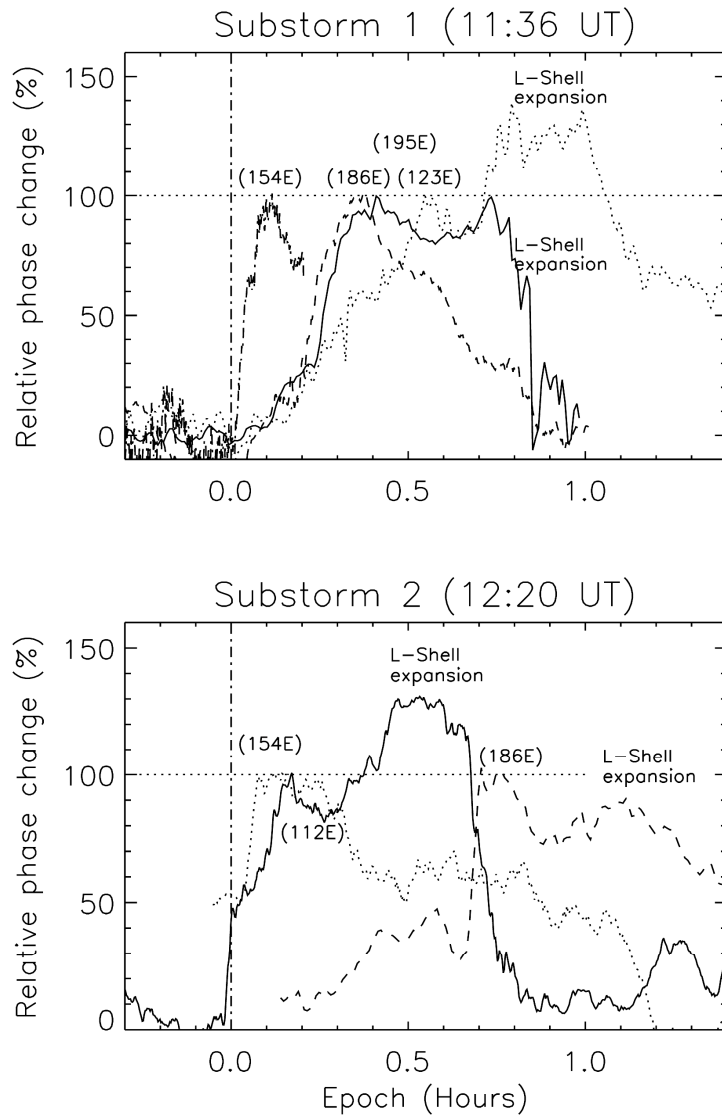


858

859 **Figure 9** The NPM-Scott Base and NPM-Casey phase change on 10-16 UT, 28 May

860 2010. Vertical lines represent the activation times of the two substorms.

861



862

863 **Figure 10.** A summary of the phase changes observed during substorm 1 (upper
 864 panel) and substorm 2 (lower panel). The phase change is expressed as a percentage,
 865 with 100% defined as the maximum phase change caused by the substorm injections.
 866 The longitude of each propagation path where it cuts the $L=6$ contour (as shown in
 867 Figure 1) is indicated, e.g., 112°E (NWC-Casey), 123°E (NWC-Scott Base), 154°E
 868 (NPM-Casey), 186°E (NPM-Scott Base), 200°E (NLK-Scott Base). The periods of
 869 expanding L -shell extent of the substorm-induced EEP are indicated.